



SnO₂ nanocrystal-Fe₂O₃ nanorod hybrid structures: an anode material with enhanced lithium storage capacity

Tao Li¹ · Tuo Xin¹ · Yanhua Ding¹ · Jiajia Zou¹ · Huanqing Liu¹ · Bing Liu¹ · Yiqian Wang¹

Received: 29 August 2018 / Revised: 15 October 2018 / Accepted: 22 October 2018 / Published online: 10 November 2018
© Springer-Verlag GmbH Germany, part of Springer Nature 2018

Abstract

Through a two-step hydrothermal method, we synthesized a metal-oxide heterostructure composed of SnO₂ nanocrystals (NCs) with a diameter of ~ 6 nm and Fe₂O₃ nanorods (NRs) with a length of ~ 200 nm and a width of ~ 9 nm. The SnO₂ NCs are well dispersed on the surface of Fe₂O₃ NRs. The effect of Fe₂O₃ NRs loading amount on the electrochemical performance of nanocomposite is investigated. The nanocomposites with less loading amount of Fe₂O₃ exhibit better electrochemical performance. The enhanced performance is attributed to the synergistic effect of two components. On one hand, the conversion reaction of SnO₂ is facilitated due to the presence of Fe₂O₃ NRs, resulting in a high capacity. On the other hand, Fe₂O₃ NRs improve the stability of electrode, promoting the cycling performance. The high loading amount of Fe₂O₃ NRs renders the aggregation of electrode materials, resulting in poor electrochemical performance. Our results demonstrate that adjusting the loading amount of metal oxides in hybrid structures is an effective strategy to enhance lithium storage capacity.

Keywords Lithium-ion batteries · SnO₂-Fe₂O₃ composites · Anode material · Synergistic effect

Introduction

Lithium-ion batteries (LIBs) are energy storage devices which exhibit high power density, long cycle life and are environmentally friendly [1–5]. They have attracted extensive attention as power sources for electric vehicles. However, the commercially used graphite anode materials do not meet the practical requirement of electric vehicles for higher energy/power density. Therefore, many investigations have been carried out to develop suitable electrode materials for fabrication of high-performance LIBs. In recent years, metal oxides have been intensively studied as potential anode materials for the next generation LIBs because of their high theoretical capacities, low cost, and eco-friendliness [6–8].

Among various metal oxides, tin oxide (SnO₂) stands out as a promising anode material due to its high theoretical

capacity, low working potential, and natural abundance [9–11]. In addition, iron oxide (Fe₂O₃) has emerged as another important anode material for LIBs due to its high theoretical capacity (~ 1007 mAh g⁻¹) [12–14]. However, like other metal oxides that can be used as anode materials for LIBs, SnO₂ and Fe₂O₃ suffer from huge volume changes during the Li⁺ insertion/extraction process, leading to critical pulverization issues. Furthermore, such volume changes result in a rapid capacity decay and poor cycle performance [15–17].

To overcome the drawback of SnO₂ and Fe₂O₃ on lithium storage, several strategies have been put forward [18–20]. Among these approaches, fabricating hybrid nanostructures of SnO₂ and Fe₂O₃ has proved to be an effective solution [21, 22]. The hybrid nanostructures benefit not only from the advantages of individual constituents but also provide synergistic effect which can enhance their electrochemical performance and simultaneously yield improved stability [21, 23, 24]. Thus, fabrication of SnO₂ and Fe₂O₃ nanomaterials into hybrid nanostructures represents a promising opportunity towards high-performance LIBs.

Herein, we report a two-step hydrothermal method to fabricate hybrid SnO₂-Fe₂O₃ composites with different loading amount of Fe₂O₃. The SnO₂ nanocrystals (NCs) with a diameter of 6 nm are well dispersed on the Fe₂O₃ nanorods (NRs) with a length of 200 nm and a width of 9 nm. When used as an

Tao Li and Tuo Xin contributed equally to this work.

✉ Bing Liu
bing_liu@qdu.edu.cn

✉ Yiqian Wang
yqwang@qdu.edu.cn

¹ College of Physics, Qingdao University, No. 308 Ningxia Road, Qingdao 266071, People's Republic of China

anode material for LIBs, the SnO₂-Fe₂O₃ composites exhibit high capacity (1234 mAh g⁻¹ at 100 mAh g⁻¹ after 200 cycles) and excellent rate performance. The enhanced electrochemical performance of SnO₂-Fe₂O₃ composites can be attributed to a positive synergistic effect of two metal oxides. The presence of Fe₂O₃ NRs promotes the conversion reaction of SnO₂, improving the specific capacity of SnO₂-Fe₂O₃ composites. Simultaneously, SnO₂ NCs effectively separate the Fe₂O₃ NRs which act as a matrix material, providing enough space for volume expansion and suppressing the aggregation of Sn nanocrystals, which increases the structural stability of electrode materials during Li⁺ insertion/extraction process. For the composites with a high loading amount of Fe₂O₃ NRs, they are prone to aggregate, finally leading to poor electrochemical performance.

Experimental

All chemicals are of analytical grade and used as received. Distilled water is used throughout all the experiments.

Synthesis of SnO₂ NCs

SnCl₄·5H₂O (0.35 g) and 0.6 g of benzimidazole were first dissolved into a mixed solution with 20 mL distilled water and 20 mL ethanol, and then transferred into a 100 mL Teflon-sealed autoclave at 180 °C for 18 h. Subsequently, the resultant precipitates were collected by centrifugation and washed with distilled water and ethanol for five times, then dried at 60 °C for 12 h. Finally, the dry powder was annealed in an ambient atmosphere at 600 °C for 3 h in a tube furnace to obtain final product.

Synthesis of SnO₂-Fe₂O₃ composites

Scheme 1 illustrates the synthesis process of SnO₂ NCs-Fe₂O₃ NRs composites. Of the synthesized SnO₂ NCs, 3.2 mmol was dispersed in a solution of 80 mL of ethanol/water (1:1 volume ratio), which was stirred for 10 min and ultrasonicated for 10 min. Then 0.96 mmol FeCl₃·6H₂O was added into the suspension under continuous stirring and 30 mmol NaOH was dissolved in 40 mL distilled water. NaOH solution was added dropwise to the suspension and the resulting mixture was placed in a 100 mL Teflon-sealed autoclave. Thereafter, the autoclave was heated at 180 °C for 18 h. After cooling to room temperature, the resultant precipitates were centrifuged, washed with distilled water and ethanol for five times, and dried in an oven at 60 °C for 12 h. Finally, the resulting sample was further heated in an ambient atmosphere at 600 °C for 3 h, referred to as SnO₂-Fe₂O₃-1. For comparison, a different loading of Fe₂O₃ (1.92 mmol) was placed into the suspension, and the resultant product was named as SnO₂-Fe₂O₃-2.

Transmission electron microscopy sample preparation

The samples of different nanostructures for transmission electron microscopy (TEM) observations were prepared by ultrasonating them in ethanol for 10 min, and dispersing a drop onto a holey-carbon-film-coated copper grid.

Material characterization

The morphologies of the as-synthesized samples were characterized by scanning electron microscope (SEM, Hitachi S-4800) and the crystal structures of the samples were analyzed by X-ray diffraction (SmartLab XRD) with Cu-Kα₁ radiation (λ = 1.5406 Å). The chemical compositions of the products were determined using an energy-dispersive X-ray spectrometer (EDX) attached to Hitachi S-4800 SEM. Bright-field (BF) images and high-resolution transmission electron microscopy (HRTEM) images were obtained on a JEOL JEM2100F transmission electron microscope with an accelerating voltage of 200 kV.

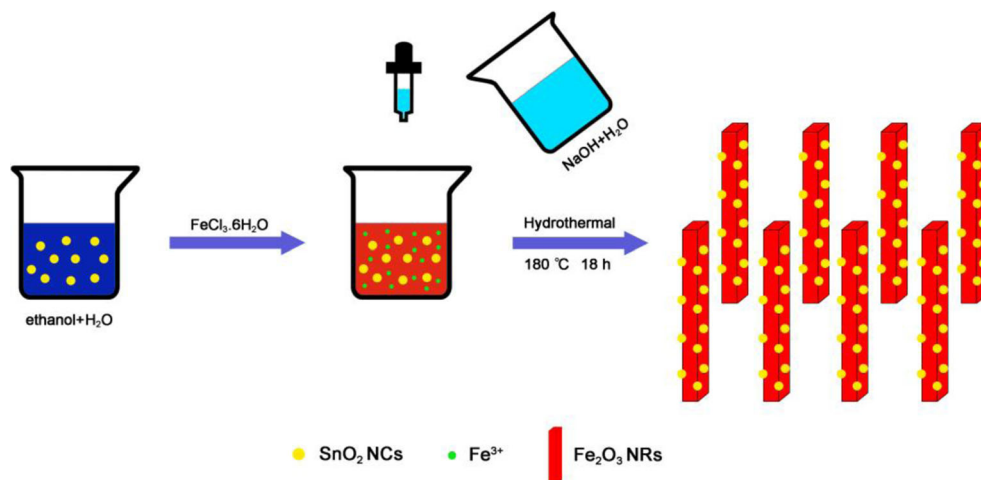
Electrochemical measurements

The electrochemical test was carried out in a CR2025-type coin cell (20 mm in diameter and 2.5 mm in thickness) with lithium metal as a counter electrode at room temperature. The working electrode was fabricated by mixing the as-prepared active materials (SnO₂ NCs, SnO₂-Fe₂O₃-1, and SnO₂-Fe₂O₃-2) with carbon black and water-soluble sodium alginate (SA) at a weight ratio (wt%) of 70:15:15 onto a pure copper foil. The electrodes were dried in a vacuum oven at 120 °C for 12 h and the cells were assembled in a glove box filled with argon with a moisture and oxygen concentration of less than 0.1 ppm. The mass loadings of SnO₂ NCs, SnO₂-Fe₂O₃-1, and SnO₂-Fe₂O₃-2 for cell testing were 1.4, 1.6, and 1.6 mg, respectively. The electrolyte consisted of 1 M LiPF₆ solution of ethylene carbonate (EC)/dimethyl carbonate (DMC)/diethyl carbonate (DEC) (1:1:1 in volume). The electrochemical performances were tested on a LAND CT2001 battery test system in a voltage range of 0.01–3.00 V at room temperature. Cyclic voltammetry (CV) measurements (over the potential range of 0.01–3.00 V at a scan rate of 0.1 mV s⁻¹) and electrochemical impedance spectroscopy (EIS) tests were performed on a Metrohm Autolab electrochemical workstation (PGSTAT 302N) with a frequency range from 100 kHz to 0.01 Hz.

Results and discussion

Figure 1 shows the XRD patterns of as-synthesized products. All the diffraction peaks for SnO₂ NCs can be exclusively indexed to tetragonal rutile SnO₂ (JCPDS no. 41-1445). For

Scheme 1 The fabrication process of SnO₂ NCs-Fe₂O₃ NRs composites



pristine SnO₂ NCs, the diffraction peaks at $2\theta = 26.6^\circ, 33.9^\circ, 37.9^\circ, 51.8^\circ, 54.8^\circ, 61.8^\circ, 65.9^\circ,$ and 71.2° are assigned to the (110), (101), (200), (211), (220), (310), (301), and (202) planes of SnO₂, respectively. For SnO₂-Fe₂O₃-1 and SnO₂-Fe₂O₃-2, all the diffraction peaks are in good agreement with those of tetragonal rutile SnO₂ (JCPDS no. 41-1445) and rhombohedral Fe₂O₃ (JCPDS no. 33-0664), respectively. No notable peaks of impurity phases are found in the XRD patterns, indicating the high purity of the products.

The morphology of as-prepared SnO₂ NCs, SnO₂-Fe₂O₃-1, and SnO₂-Fe₂O₃-2 was investigated by SEM. Figure 2a displays a typical SEM image of SnO₂ NCs, showing that the NCs pile together, with a diameter of 5–10 nm. The agglomeration of NCs could give rise to poor cycling performance. Figure 2b shows a typical SEM image of SnO₂-Fe₂O₃-1, which is assembled by SnO₂ NCs and Fe₂O₃ NRs. The SnO₂ NCs (average diameter of 6 nm) are dispersed on the surface of Fe₂O₃ NRs (average length of 200 nm and average width of 9 nm). The surface roughness of Fe₂O₃ NRs is largely increased through the combination of SnO₂ NCs and Fe₂O₃ NRs, ensuring their full contact with electrolyte. The inset of

Fig. 2b is the EDX spectrum of SnO₂-Fe₂O₃-1. The EDX spectrum shows that the as-prepared composites are composed of Sn, O, and Fe. Quantification of the EDX spectrum reveals that the atomic ratio of Sn and Fe in the SnO₂-Fe₂O₃-1 product is 1:5, indicating that the molar ratio of SnO₂ and Fe₂O₃ is 1:2.5. Figure 2c shows a typical SEM image of SnO₂-Fe₂O₃-2 composite. From Fig. 2c, it can be clearly seen that the composites show an aggregation tendency, which is extremely detrimental to the cycling performance of LIBs. Simultaneously, some SnO₂ NCs attach to Fe₂O₃ NRs. The SnO₂ NCs and Fe₂O₃ NRs are densely packed, where the SnO₂ NCs are 5–10 nm in diameter and Fe₂O₃ NRs are 20–30 nm in width. From EDX spectrum in inset of Fig. 2c, it can be seen that the composites consist of three elements (Sn, O, and Fe). Quantification of the EDX spectrum demonstrates that the atomic ratio of Sn and Fe in the SnO₂-Fe₂O₃-2 product is 1:16, indicating that the molar ratio of SnO₂ and Fe₂O₃ is 1:8.

The microstructure of three samples was extensively examined by TEM. Figure 3a presents a typical BF TEM image of SnO₂ NCs. It clearly shows that the diameter of the NCs is 5–10 nm, which is consistent with the SEM results. Moreover, the agglomeration phenomenon of NCs is also observed. Figure 3b shows a typical HRTEM image of the SnO₂ NCs, from which the (110) lattice spacing is measured to be 3.35 Å, consistent with that of the bulk SnO₂. Figure 3c presents the size distribution of SnO₂ NCs, showing that the as-prepared SnO₂ NCs are relatively uniform, with an average diameter of 6 nm. Figure 3d displays a typical BF TEM image of SnO₂-Fe₂O₃-1 composite, which consists of SnO₂ NCs and Fe₂O₃ NRs. As seen from the BF TEM image, SnO₂ NCs are well decorated on the surfaces of Fe₂O₃ NRs. The diameter of SnO₂ NCs is the same as that of pure SnO₂ NCs. The crystal lattice spacings measured from HRTEM image are 3.35 and 3.68 Å, as indicated in Fig. 3e, which correspond to (110) of SnO₂ NCs and (01 $\bar{1}$ 2) of Fe₂O₃ NRs, respectively. In addition, it clearly shows that the SnO₂ NCs (labeled by red circle)

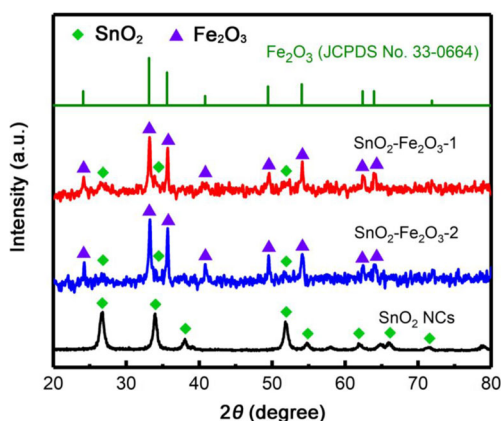


Fig. 1 XRD patterns of the pristine SnO₂ NCs, SnO₂-Fe₂O₃ composites with different loadings of Fe₂O₃, and the standard XRD pattern of the rhombohedral Fe₂O₃

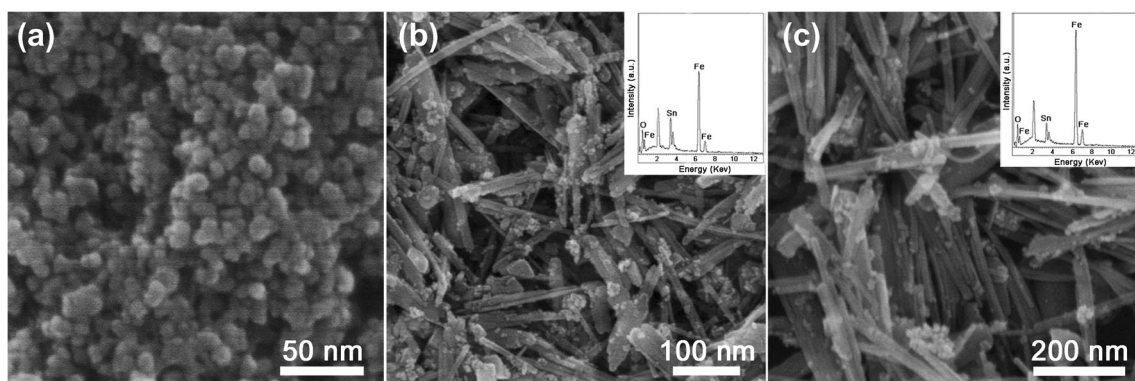
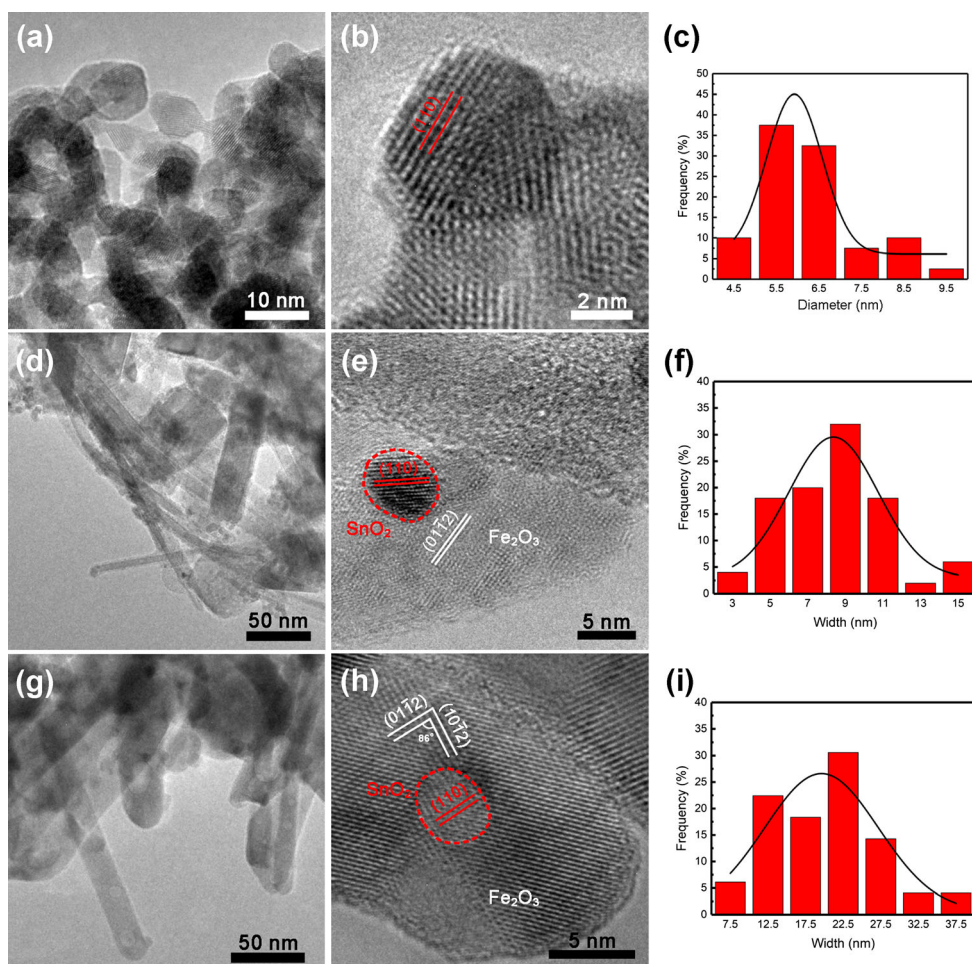


Fig. 2 Typical SEM images of as-synthesized SnO₂ NCs (a), as-synthesized SnO₂-Fe₂O₃-1 (b), and as-synthesized SnO₂-Fe₂O₃-2 (c). Inset in b shows the EDX spectrum of SnO₂-Fe₂O₃-1. Inset in c shows the EDX spectrum of SnO₂-Fe₂O₃-2

are dispersed on the surface of Fe₂O₃ NRs. Figure 3f shows a typical width distribution of Fe₂O₃ NRs in the SnO₂-Fe₂O₃-1 composites, with an average width of about 9 nm. The TEM image (Fig. 3g) displays that the SnO₂-Fe₂O₃-2 composites are assembled from SnO₂ NCs and Fe₂O₃ NRs. The size of SnO₂ NCs is 5–10 nm which is similar to those of the other two samples. Figure 3h is the corresponding HRTEM image

of SnO₂-Fe₂O₃-2. The SnO₂ NCs (labeled by red circle) adhere to the Fe₂O₃ NRs. The measured lattice spacing of about 3.71 Å corresponds to that of (01 $\bar{1}$ 2) plane of Fe₂O₃ NRs. Additionally, the crystal lattice spacing of about 3.35 Å is in agreement with that of (110) plane of SnO₂ NCs. As shown in Fig. 3i, the average width of Fe₂O₃ NRs in the SnO₂-Fe₂O₃-2 composites is about 20 nm. The average width of Fe₂O₃ NRs

Fig. 3 Typical TEM images of SnO₂ NCs (a, b); SnO₂-Fe₂O₃-1 (d, e); SnO₂-Fe₂O₃-2 (g, h). Size distribution of SnO₂ NCs obtained from analysis of 100 SnO₂ NCs (c); width distribution of Fe₂O₃ NRs in SnO₂-Fe₂O₃-1 (f), and SnO₂-Fe₂O₃-2 (i) obtained from statistical analysis of 100 Fe₂O₃ NRs



in $\text{SnO}_2\text{-Fe}_2\text{O}_3\text{-2}$ is larger than that of Fe_2O_3 in $\text{SnO}_2\text{-Fe}_2\text{O}_3\text{-1}$, indicating that the width of Fe_2O_3 NRs increases with the concentration of iron precursor.

To investigate the electrochemical performance of the as-synthesized products, they were used as anode materials for LIBs. In LIBs, the lithium storage mechanism can be divided into three models: alloy model, displacement model, and intercalation model, respectively. Alloy model includes two-step reaction. In the first process, metal oxide reacts with Li^+ and is reduced to metal, which is generally irreversible. In the next process, the metal further reacts with Li^+ to form the Li-metal alloy. In the displacement model, the mechanism involves the reversible formation and decomposition of Li_2O during the charge-discharge process. For the intercalation model, Li -ion can insert/extract in the open channels of metal oxides with layered structures [25]. During the Li^+ insertion/extraction process, the SnO_2 electrode follows the alloy model, while Fe_2O_3 electrode follows the displacement model. The lithium storage mechanism of SnO_2 involves a two-step reaction,

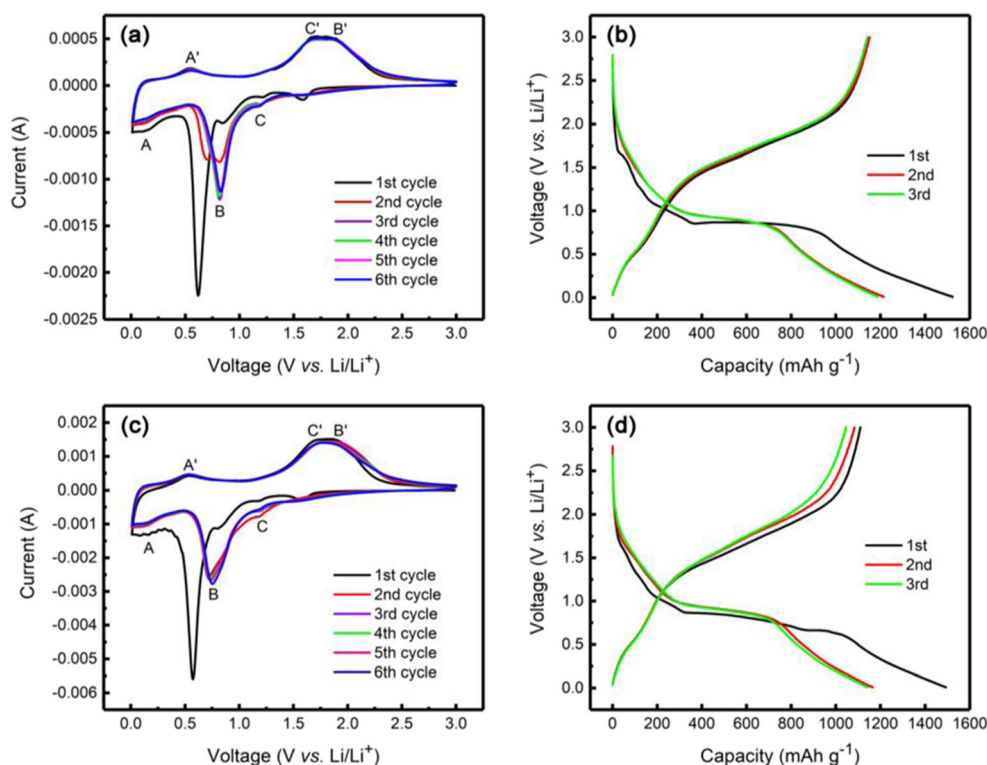


When Fe_2O_3 is used as the anode material for LIBs, the electrochemical process can be described as the follow equation:



The phase changes and ion diffusion process of the electrode materials in the charge-discharge process were investigated by CV curves. Figure 4a, c shows CV curves of the $\text{SnO}_2\text{-Fe}_2\text{O}_3\text{-1}$ electrode and $\text{SnO}_2\text{-Fe}_2\text{O}_3\text{-2}$ electrode for the first six CV cycles in the potential range of 0.01–3.00 V at a scan rate of 0.5 mV s^{-1} , in which a similar electrochemical redox process can be observed. From Fig. 4a, a reduction peak at around 0.62 V (versus Li/Li^+) is observed in the first cycle and disappears in subsequent cycles, which could be ascribed to the decomposition of the electrode and the formation of SEI. Moreover, the reduction peak A (0.12 V) and oxidation peak A' (0.53 V) correspond to reversible alloying reaction of the Sn alloy, as shown in Eq. (2) [26, 27]. The reduction peak B (0.82 V) is attributed to the Li^+ insertion into Fe_2O_3 and the formation of Li_2O , as given in Eq. (3). The oxidation peak B' (1.85 V) corresponds to the formation of Fe^{3+} from Fe^0 [28, 29]. The peak C (1.20 V) is associated with the reduction from SnO_2 to Sn and the simultaneous formation of Li_2O in Eq. (1). The oxidation peak C' (1.70 V) is assigned to the excellent reversibility of the conversion reaction of SnO_2 , as described in Eq. (1). In the subsequent reduction and oxidation scans, the CV curves almost overlap, implying good reversibility of the electrochemical reactions. As shown in Fig. 4c, the CV curves of $\text{SnO}_2\text{-Fe}_2\text{O}_3\text{-2}$ are analogical to the CV curves of $\text{SnO}_2\text{-Fe}_2\text{O}_3\text{-1}$. Figure 4b, d shows the galvanostatic discharge-charge profiles of $\text{SnO}_2\text{-Fe}_2\text{O}_3\text{-1}$ electrode and $\text{SnO}_2\text{-Fe}_2\text{O}_3\text{-2}$ electrode during the 1st, 2nd, and 3rd cycles at a current density of 100 mA g^{-1} over a voltage range from

Fig. 4 **a** CV curves of $\text{SnO}_2\text{-Fe}_2\text{O}_3\text{-1}$ at 0.1 mV s^{-1} ; **b** discharge-charge profiles of $\text{SnO}_2\text{-Fe}_2\text{O}_3\text{-1}$ at a current density of 100 mA g^{-1} ; **c** CV curves of $\text{SnO}_2\text{-Fe}_2\text{O}_3\text{-2}$ at 0.1 mV s^{-1} ; **d** discharge-charge profiles of $\text{SnO}_2\text{-Fe}_2\text{O}_3\text{-2}$ at a current density of 100 mA g^{-1}



0.01 to 3.0 V, respectively. The initial discharge and charge capacity of $\text{SnO}_2\text{-Fe}_2\text{O}_3\text{-1}$ are 1523 and 1151 mAh g^{-1} , with an initial coulombic efficiency of 75.6%. The initial 24.4% capacity loss is mainly ascribed to the formation of the solid electrolyte interphase (SEI) layer and decomposition of the electrolyte. Compared with $\text{SnO}_2\text{-Fe}_2\text{O}_3\text{-2}$, the $\text{SnO}_2\text{-Fe}_2\text{O}_3\text{-1}$ electrode exhibits the discharge/charge capacities of 1214/1151 and 1186/1141 mAh g^{-1} in the 2nd and 3rd cycles, respectively, which exhibit high coulombic efficiency of 94.8 and 96.2%. These values are higher than those of $\text{SnO}_2\text{-Fe}_2\text{O}_3\text{-2}$, which is due to the dense packing of SnO_2 NCs and Fe_2O_3 NRs in the $\text{SnO}_2\text{-Fe}_2\text{O}_3\text{-2}$ composite.

Figure 5a shows the comparative cycling performances of as-synthesized SnO_2 NCs, $\text{SnO}_2\text{-Fe}_2\text{O}_3\text{-1}$, and $\text{SnO}_2\text{-Fe}_2\text{O}_3\text{-2}$ composites at a current density of 100 mA g^{-1} . The reversible capacity of the SnO_2 NCs electrode gradually decreases and reserves only 55 mAh g^{-1} after 100 cycles, indicating that the electrode material suffers from severe pulverization, which leads to the inferior electrochemical performance. By comparison, $\text{SnO}_2\text{-Fe}_2\text{O}_3\text{-1}$ and $\text{SnO}_2\text{-Fe}_2\text{O}_3\text{-2}$ composites exhibit greatly improved capacity and cycling performance. For $\text{SnO}_2\text{-Fe}_2\text{O}_3\text{-1}$, the specific capacity decreases in the first 80 cycles and increases from the 80th to the 200th cycle. A similar phenomenon has been observed in other transition metal oxides and the increase of capacity upon cycling is generally attributed to the reversible growth of a polymeric gel-like layer caused by kinetically activated electrolyte degradation [30]. The gel-like layer can store Li^+ in the activation

process of the electrode through a so-called pseudo-capacitance behavior [31]. After 200 cycles, the $\text{SnO}_2\text{-Fe}_2\text{O}_3\text{-1}$ composites retain a reversible capacity of 1234 mAh g^{-1} . The $\text{SnO}_2\text{-Fe}_2\text{O}_3\text{-2}$ composites only retain the specific capacity of 184 mAh g^{-1} , which is much lower than that of $\text{SnO}_2\text{-Fe}_2\text{O}_3\text{-1}$ composites. The $\text{SnO}_2\text{-Fe}_2\text{O}_3\text{-1}$ electrode shows superior electrochemical performance, which demonstrates that the presence of Fe_2O_3 NRs increases the specific capacity of $\text{SnO}_2\text{-Fe}_2\text{O}_3\text{-1}$. Meanwhile, the loading of Fe_2O_3 is crucial for the lithium storage capacity of these samples. The higher Fe_2O_3 loading amount makes electrode materials easier to aggregate during the Li^+ insertion/extraction process, which inhibits the electrochemical performance. Hence, a certain number of SnO_2 NCs effectively separate Fe_2O_3 NRs, which leaves enough space for the volume expansion, contributing to the cycle performance.

During the charging-discharging process, the SnO_2 electrode materials follow the alloy model, including two key processes. The conversion reaction [Eq. (1)] of SnO_2 is generally considered irreversible and does not contribute to the reversible capacity during the Li^+ insertion/extraction process. The theoretical capacity of 792 mAh g^{-1} is calculated based on Eq. (2) [32]. The theoretical capacity of Fe_2O_3 is calculated to be 1007 mAh g^{-1} , based on Eq. (3). The theoretical capacity for $\text{SnO}_2\text{-Fe}_2\text{O}_3$ composites can be calculated using the following equation.

$$C_{\text{SnO}_2\text{-Fe}_2\text{O}_3} = C_{\text{SnO}_2} \times M_{\text{SnO}_2} + C_{\text{Fe}_2\text{O}_3} \times M_{\text{Fe}_2\text{O}_3} \quad (4)$$

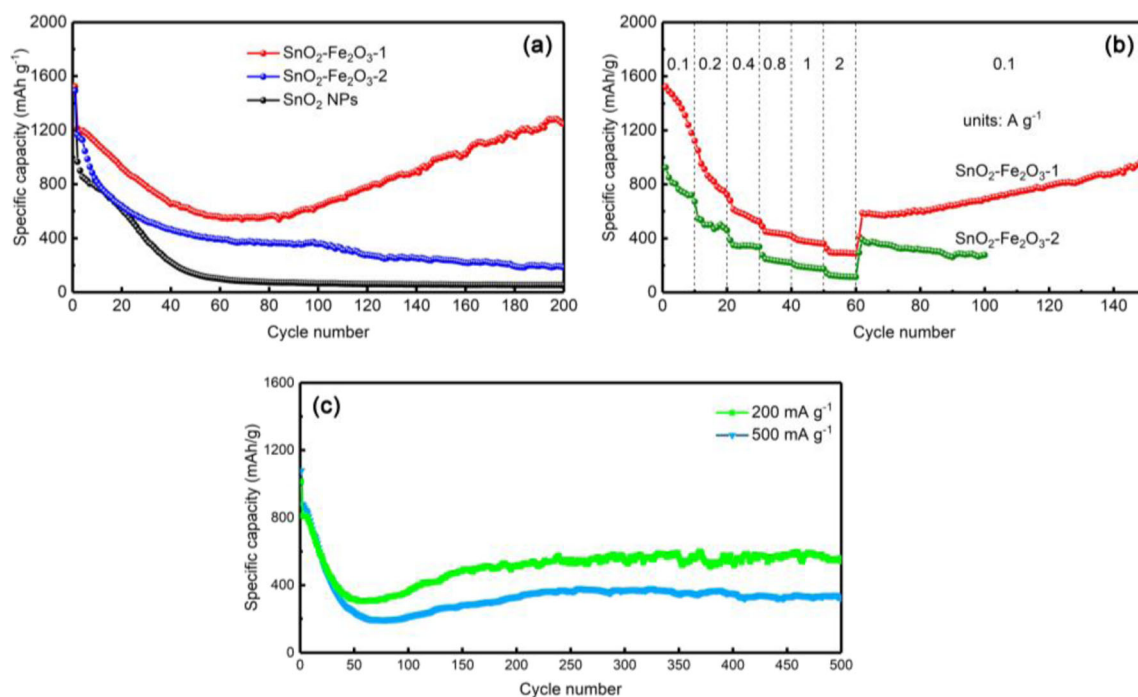


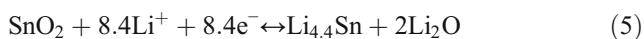
Fig. 5 **a** Cycling performances of SnO_2 NCs, $\text{SnO}_2\text{-Fe}_2\text{O}_3\text{-1}$, and $\text{SnO}_2\text{-Fe}_2\text{O}_3\text{-2}$ composites at a current density of 100 mA g^{-1} ; **b** rate performances of $\text{SnO}_2\text{-Fe}_2\text{O}_3\text{-1}$ and $\text{SnO}_2\text{-Fe}_2\text{O}_3\text{-2}$ composites at

various current rates; **c** high-rate long-term cycle performances of $\text{SnO}_2\text{-Fe}_2\text{O}_3\text{-1}$ at 200 mA g^{-1} and 500 mA g^{-1} , respectively

Table 1 Comparison of recent work on metal oxide-based materials as anodes for LIBs

Sample	Current density (mA g ⁻¹)	Cycle number	Specific capacity after cycles (mAh g ⁻¹)	Ref.
SnO ₂ @C nanospheres embedded in carbon film structure	500	200	881	[9]
SnO ₂ -Fe ₂ O ₃ @C composites	400	380	1000	[21]
SnO ₂ -Fe ₂ O ₃ heterostructures	400	50	325	[22]
SnO ₂ /Fe ₂ O ₃ /RGO	200	220	883	[23]
SnO ₂ nanoparticles	375	100	564	[27]
Branched α-Fe ₂ O ₃ /SnO ₂	1000	30	260	[34]
Core-shell α-Fe ₂ O ₃ /SnO ₂ heterostructures	100	30	341	[35]
Porous α-Fe ₂ O ₃ @TiO ₂ NRs	100	46	449.3	[36]
SnO ₂ NCs-Fe ₂ O ₃ NRs-1	100, 200, 500	200, 500, 500	1234, 556, 326	This work

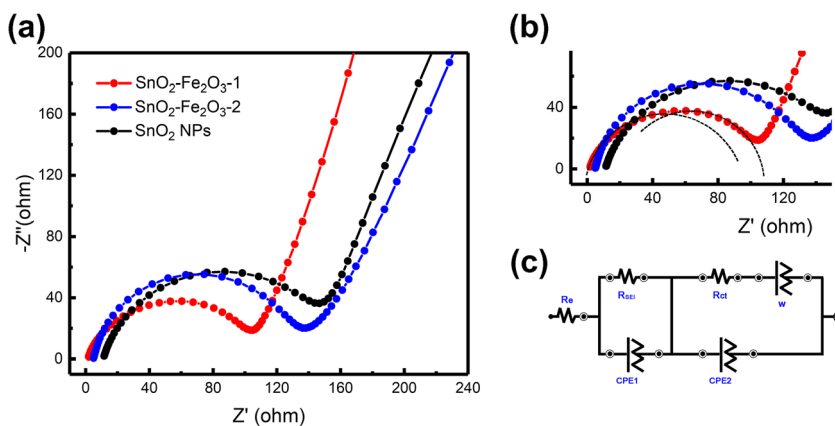
where $C_{\text{SnO}_2\text{-Fe}_2\text{O}_3}$, C_{SnO_2} , and $C_{\text{Fe}_2\text{O}_3}$ correspond to the theoretical capacity of SnO₂-Fe₂O₃ nanocomposites, SnO₂ NCs, and Fe₂O₃ NRs, respectively. M_{SnO_2} and $M_{\text{Fe}_2\text{O}_3}$ are the molar fraction of SnO₂ and Fe₂O₃ in the SnO₂-Fe₂O₃ composites, respectively. Hence, the theoretical capacity of the as-synthesized SnO₂-Fe₂O₃-1 is estimated to be 945 mAh g⁻¹, which is lower than that of the experimental value. Recently, it has been proposed that the conversion reaction [Eq. (1)] proves to be reversible for nanometer-sized SnO₂ particles [33]. Moreover, NCs like Fe nanocrystals can catalyze the decomposition of Li₂O, enhancing the reversibility of the conversion reaction of SnO₂ [34]. Hence, the theoretical specific capacity of SnO₂ can increase from 792 to 1494 mAh g⁻¹. The theoretical capacity of SnO₂-Fe₂O₃-1 increases to 1146 mAh g⁻¹, which can explain the high lithium storage capacity measured for SnO₂-Fe₂O₃-1. The overall electrochemical reaction of SnO₂ NCs electrode should be described as:



To unveil the rate capabilities of the samples for lithium storage, the rate performances were carried out at different specific currents, as shown in Fig. 5b. At specific currents of

0.1, 0.2, 0.4, 0.8, 1, and 2 A g⁻¹, the SnO₂-Fe₂O₃-1 electrode exhibits reversible capacities of 1431, 806, 564, 443, 373, and 297 mAh g⁻¹, respectively. These values are all higher than those of SnO₂-Fe₂O₃-2. When the current is reduced to 0.1 A g⁻¹, an average capacity of 993 mAh g⁻¹ after 150 cycles is recovered, which demonstrates an excellent rate performance of SnO₂-Fe₂O₃-1. The enhanced charge/discharge capacity and rate performance of SnO₂-Fe₂O₃-1 can be ascribed to the following factors. On one hand, nanometer-sized SnO₂ NCs and the positive synergistic effect of SnO₂ and Fe₂O₃ can promote the conversion reaction of SnO₂, leading to high specific capacity. On the other hand, SnO₂ NCs effectively separate the Fe₂O₃ NRs acting as a matrix material, leaving enough space for volume expansion and suppressing the aggregation of Sn nanocrystals, which improves the stability of electrode materials during the charging-discharging process. Figure 5c shows long-term cycle performances of SnO₂-Fe₂O₃-1 at 200 and 500 mA g⁻¹, respectively. Impressively, the capacity declines first and then increases during the charging-discharging process, which is consistent with the cycling performance of SnO₂-Fe₂O₃-1 at a current density of 100 mA g⁻¹. As shown in Fig. 5c, the reversible capacity reach 556 and 326 mAh g⁻¹, respectively, which further confirms the superior electrochemical performance of SnO₂-

Fig. 6 a EIS of SnO₂ NCs, SnO₂-Fe₂O₃-1, and SnO₂-Fe₂O₃-2 composites; b the magnified image of EIS; c the equivalent electrical circuit



Fe₂O₃-1. The remarkable performance of SnO₂-Fe₂O₃-1 was emphasized in comparison with other reported electrodes, as listed in Table 1. It can be found that the performance of the SnO₂-Fe₂O₃-1 composite is superior to most of the previously reported results.

To further investigate their electrochemical reaction kinetics, EIS measurements of three different nanostructures were carried out, as shown in Fig. 6a. It shows that Nyquist plots consist of two semicircles (labeled by dashed lines in Fig. 6b) at high and medium frequency, and a straight line at low frequency. The latter is related to the Warburg impedance, indicating the solid state diffusion of the Li⁺ in the electrode. The semicircle in the high frequency region is attributed to the Li⁺ migration resistance through the SEI layer (R_{SEI}). The semicircle in the medium frequency region corresponds to the charge transfer resistance through electrode/electrolyte (R_{ct}). According to the equivalent circuit (Fig. 6c), the resistance of SnO₂-Fe₂O₃-1 composites ($R_{ct} = 105 \Omega$) is smaller than those of SnO₂ NCs ($R_{ct} = 154 \Omega$) and SnO₂-Fe₂O₃-2 composites ($R_{ct} = 131 \Omega$), which implies that Li⁺ and electrons can pass through the interface of electrode/electrolyte more easily due to the introduction of Fe₂O₃ NRs. The deposition of SnO₂ NCs on the Fe₂O₃ NRs increases the contact area between the electrode and electrolyte. The successful interaction of SnO₂ and Fe₂O₃ confirms that Fe₂O₃ NRs in hybrid anode materials not only improve the stability of the electrode, but also effectively shorten the length of Li⁺ diffusion and electron transport during the repeated Li⁺ insertion/extraction process.

Conclusions and perspectives

In summary, SnO₂-Fe₂O₃ hybrids were synthesized using a simple two-step hydrothermal method. SnO₂ NCs are bound to the surface of the Fe₂O₃ NRs to suppress the aggregation of Sn NCs during the Li insertion/extraction process. When used as anode materials, the SnO₂-Fe₂O₃ composites show high specific capacity, long cycling lifespan, and excellent rate performance. The excellent electrochemical behavior is attributed to the unique structure of the electrode materials and positive synergistic effect between the two metal oxides. Our work can provide a new pathway to the development of high-performance LIBs.

Funding information We would like to thank the financial support from the National Key Basic Research Development Program of China (Grant No.: 2012CB722705), the National Natural Science Foundation of China (Grant No.: 10974105), the Natural Science Foundation for Outstanding Young Scientist in Shandong Province (Grant no.: JQ201002), and High-end Foreign Experts Recruitment Programs (Grant Nos.: GDW20173500154, GDW20163500110). Y. Q. Wang would also like to thank the financial support from the Top-notch Innovative Talent Program of Qingdao City (Grant No.: 13-CX-08), the Taishan Scholar Program of Shandong Province, Qingdao International Center for Semiconductor Photoelectric Nanomaterials, and Shandong Provincial

University Key Laboratory of Optoelectrical Material Physics and Devices.

References

1. Tarascon JM, Armand M (2001) Issues and challenges facing rechargeable lithium batteries. *Nature* 414(6861):359–367
2. Yoshino A (2012) The birth of the lithium-ion battery. *Angew Chem Int Ed* 51(24):5798–5800
3. Chen YM, Yu L, Lou XW (2016) Hierarchical tubular structures composed of Co₃O₄ hollow nanoparticles and carbon nanotubes for lithium storage. *Angew Chem Int Ed* 55(20):5990–5993
4. Goodenough JB, Kim Y (2010) Challenges for rechargeable Li batteries. *Chem Mater* 22(3):587–603
5. Liu B, Cao MH, Zhao XY, Tian Y, Hu CW (2013) Facile synthesis of ultrafine carbon-coated SnO₂ nanoparticles for high-performance reversible lithium storage. *J Power Sources* 243:54–59
6. Reddy MV, Subba Rao GV, Chowdari BVR (2013) Metal oxides and oxysalts as anode materials for Li ion batteries. *Chem Rev* 113(7):5364–5457
7. Wang ZY, Zhou L, Lou XW (2012) Metal oxide hollow nanostructures for lithium-ion batteries. *Adv Mater* 24(14):1903–1911
8. Chen JS, Archer LA, Lou XW (2011) SnO₂ hollow structures and TiO₂ nanosheets for lithium-ion batteries. *J Mater Chem* 21(27):9912–9924
9. Ao X, Jiang JJ, Ruan YJ, Li ZS, Zhang Y, Sun JW, Wang CD (2017) Honeycomb-inspired design of ultrafine SnO₂@C nanospheres embedded in carbon film as anode materials for high performance lithium- and sodium-ion battery. *J Power Sources* 359:340–348
10. Pan D, Wan N, Ren Y, Zhang WF, Lu X, Wang YS, Hu YS, Bai Y (2017) Enhanced structural and electrochemical stability of self-similar rice-shaped SnO₂ nanoparticles. *ACS Appl Mater Interfaces* 9(11):9747–9755
11. Han S, Jang B, Kim T, Oh SM, Hyeon T (2005) Simple synthesis of hollow tin dioxide microspheres and their application to lithium-ion battery anodes. *Adv Funct Mater* 15(11):1845–1850
12. Reddy MV, Yu T, Sow CH, Shen ZX, Lim CT, Subbarao GV, Chowdari BVR (2007) α -Fe₂O₃ nanoflakes as an anode material for Li-ion batteries. *Adv Funct Mater* 17(15):2792–2799
13. Jiang TC, Bu FX, Feng XX, Shakir I, Hao GL, Xu YX (2017) Porous Fe₂O₃ nanoframeworks encapsulated within three-dimensional graphene as high-performance flexible anode for lithium-ion battery. *ACS Nano* 11(5):5140–5147
14. Wang B, Chen JS, Wu HB, Wang Z, Lou XW (2011) Quasiemulsion-templated formation of α -Fe₂O₃ hollow spheres with enhanced lithium storage properties. *J Am Chem Soc* 133(43):17146–17148
15. Li JX, Zhao Y, Wang N, Guan LH (2011) A high performance carrier for SnO₂ nanoparticles used in lithium ion battery. *Chem Commun* 47(18):5238–5240
16. Yin XM, Li CC, Zhang M, Hao QY, Liu S, Chen LB, Wang TH (2010) One-step synthesis of hierarchical SnO₂ hollow nanostructures via self-assembly for high power lithium ion batteries. *J Phys Chem C* 114(17):8084–8088
17. Wu QH, Zhao RF, Zhang X, Li WL, Xu RH, Diao GW, Chen M (2017) Synthesis of flexible Fe₃O₄/C nanofibers with buffering volume expansion performance and their application in lithium-ion batteries. *J Power Sources* 359:7–16
18. Yan Y, Du FH, Shen XP, Ji ZY, Zhou H, Zhu GX (2014) Porous SnO₂-Fe₂O₃ nanocubes with improved electrochemical performance for lithium ion batteries. *Dalton Trans* 43(46):17544–17550

19. Li HQ, Zhou HS (2012) Enhancing the performances of Li-ion batteries by carbon-coating: present and future. *Chem Commun* 48(9):1201–1217
20. Hu RZ, Ouyang YP, Liang T, Wang H, Liu J, Chen J, Yang CH, Yang LC, Zhu M (2017) Stabilizing the nanostructure of SnO₂ anodes by transition metals: a route to achieve high initial coulombic efficiency and stable capacities for lithium storage. *Adv Mater* 29(13):1605006
21. Guo JX, Chen L, Wang GJ, Zhang X, Li FF (2014) In situ synthesis of SnO₂-Fe₂O₃@polyaniline and their conversion to SnO₂-Fe₂O₃@C composite as fully reversible anode material for lithium-ion batteries. *J Power Sources* 246:862–867
22. Wang YL, Xu JJ, Wu H, Xu M, Peng Z, Zheng GF (2012) Hierarchical SnO₂-Fe₂O₃ heterostructures as lithium-ion battery anodes. *J Mater Chem* 22(41):21923
23. Lee K, Shin S, Degen T, Lee W, Yoon YS (2017) In situ analysis of SnO₂/Fe₂O₃/RGO to unravel the structural collapse mechanism and enhanced electrical conductivity for lithium-ion batteries. *Nano Energy* 32:397–407
24. Li Y, Yu SL, Yuan TZ, Yan M, Jiang YZ (2015) Rational design of metal oxide nanocomposites anodes for advanced lithium ion batteries. *J Power Sources* 282:1–8
25. Wei W, Wang ZH, Liu Z, Liu Y, He L, Chen DZ, Umar A, Guo L, Li JH (2013) Metal oxide hollow nanostructures: fabrication and Li storage performance. *J Power Sources* 238:376–387
26. Zhou XS, Wan LJ, Guo YG (2013) Binding SnO₂ nanocrystals in nitrogen-doped graphene sheets as anode materials for lithium-ion batteries. *Adv Mater* 25:152–2157
27. Etacheri V, Seisenbaeva GA, Caruthers J, Daniel G, Nedelec JM, Kessler Vadim G, Pol Vilas G (2015) Ordered network of interconnected SnO₂ nanoparticles for excellent lithium-ion storage. *Adv Energy Mater* 5(5):1401289
28. Liu H, Wang GX, Park J, Wang JZ, Liu HK, Zhang C (2009) Electrochemical performance of α -Fe₂O₃ nanorods as anode material for lithium-ion cells. *Electrochim Acta* 54(6):1733–1736
29. Wang X, Xiao Y, Hu CW, Cao MH (2014) A dual strategy for improving lithium storage performance, a case of Fe₂O₃. *Mater Res Bull* 59:162–169
30. Zhou L, Wu HB, Zhu T, Lou XW (2012) Facile preparation of ZnMn₂O₄ hollow microspheres as high-capacity anodes for lithium-ion batteries. *J Mater Chem* 22(3):827–829
31. Sun XL, Si WP, Liu XH, Deng JW, Xi LX, Liu LF, Yan CL, Schmidt OG (2014) Multifunctional Ni/NiO hybrid nanomembranes as anode materials for high-rate Li-ion batteries. *Nano Energy* 9:168–175
32. Wang C, Du GH, Stahl K, Huang HX, Zhong YJ, Jiang JZ (2012) Ultrathin SnO₂ nanosheets: oriented attachment mechanism, nonstoichiometric defects, and enhanced lithium-ion battery performances. *J Phys Chem C* 116(6):4000–4011
33. Jiang BB, He YJ, Li B, Zhao SQ, Wang S, He YB, Lin ZQ (2017) Polymer-templated formation of polydopamine-coated SnO₂ nanocrystals: anodes for cyclable lithium-ion batteries. *Angew Chem Int Ed* 56(7):1869–1872
34. Zhou WW, Cheng CW, Liu JP, Tay YY, Jiang J, Jia XT, Zhang JX, Gong H, Hng HH, Yu T, Fan HJ (2011) Epitaxial growth of branched α -Fe₂O₃/SnO₂ nano-heterostructures with improved lithium-ion battery performance. *Adv Funct Mater* 21(13):2439–2445
35. Li YF, Hu YJ, Jiang H, Hou XY, Li CZ (2013) Phase-segregation induced growth of core-shell α -Fe₂O₃/SnO₂ heterostructures for lithium-ion battery. *CrystEngComm* 15(34):6715–6721
36. Zhang X, Chen HX, Xie YP, Guo JX (2014) Ultralong life lithium-ion battery anode with superior high-rate capability and excellent cyclic stability from mesoporous Fe₂O₃@TiO₂ core-shell nanorods. *J Mater Chem A* 2(11):3912–3918